A crank-kinematics based engine cylinder pressure reconstruction model

Article (Accepted Version)

A CRANK-KINEMATICS BASED ENGINE CYLINDER PRESSURE RECONSTRUCTION MODEL

by

J.F. Dunne and C. Bennett

Department of Engineering and Design
School of Engineering and Informatics
University of Sussex, Falmer, Brighton, BN1 9QT, UK.
* Corresponding author: E-mail: j.f.dunne@sussex.ac.uk

ABSTRACT

A new inverse model is proposed for reconstructing steady-state and transient engine cylinder pressure using measured crank kinematics. An adaptive nonlinear time-dependent relationship is assumed between windowed-subsections of cylinder pressure and measured crank kinematics in a time-domain format (rather than in crank-angle-domain). This relationship comprises a linear sum of four separate nonlinear functions of crank jerk, acceleration, velocity, and crank angle. Each of these four nonlinear functions is obtained at each time instant by fitting separate *m*-term Chebychev polynomial expansions, where the total 4*m* instantaneous expansion coefficients are found using a standard (over-determined) linear least-square solution method. A convergence check on the calibration accuracy shows this initially improves as more Chebychev polynomial terms are used, but with further increase, the over-determined system becomes singular. Optimal accuracy Chebychev expansions are found to be of degree *m*=4, using 90 or more cycles of engine data to fit the model. To confirm the model accuracy in predictive mode, a defined measure is used, namely the *'calibration peak pressure error'*. This measure allows effective *a priori* exclusion of occasionally unacceptable predictions. The method is tested using varying speed data taken from a 3-cylinder DISI engine fitted with cylinder pressure sensors, and a high resolution shaft encoder. Using appropriately-filtered crank kinematics (plus the 'calibration peak pressure error'), the model produces fast and accurate predictions for previously unseen data. Peak pressure predictions are consistently within 6.5% of target, whereas locations of peak pressure are consistently within ± 2.7˚ CA. The computational efficiency makes it very suitable for real-time implementation.

22 main-section pages (double-spaced) 33 references 15 Figures No Appendices

1. INTRODUCTION

Closed-loop combustion control on multi-cylinder IC engines offers an important way to improve fuel economy, and thereby reduce CO_2 emissions [1][2][3]. Combustion control also offers a potentially inexpensive route to reduce harmful tailpipe emissions, particularly for HD diesel [4]. The importance and value of knowledge of in-cylinder pressure in terms of combustion parameters has been reviewed in [5]. In general, combustion control requires knowledge of the instantaneous cylinder pressures, particularly for gasoline engines, which show considerable cycle-by-cycle variability owing to the stochastic nature of combustion involved pre-mixed air and fuel. Direct measurement of cylinder pressure is achievable using available in-cylinder pressure sensors, fitted routinely in special conditions such as for engine development and test programmes, or in high value motor sport. Commercial pressure sensors are generally designed to endure very hostile in-cylinder conditions for a relatively limited duration of use without need of servicing and recalibration. However direct sensing, involving use of commercial pressure sensors on production engines, is generally still very problematic. This difficulty stems from the relatively high sensor cost compared with the unit cost of the engine; from durability issues which pose OBD and in-service cost difficulties. And from packaging issues, namely the difficulty of finding the space on a very crowded cylinder head to fit the sensor. This packaging issue is increasingly problematic, on very compact lightweight combustion engines needed for Hybrid Electric Vehicles. Alternative direct sensing methods include the use of crank-head bolts and, specifically for SI engines, exploiting spark-plug ionisation current by building a relationship to cylinder pressure.

Attempts have been made over the past two decades to find alternative ways to sense engine cylinder pressure, either directly using different types of sensor technology, or to indirectly reconstruct cylinder pressure using other sensors already fitted to the engine [6].

The use of indirect methods involves construction of an inverse dynamic model of the causal relationship between cylinder pressure and responses such as crank kinematics, engine head or block vibration or acoustic structural responses. The aim is when such models are fed with instantaneous response measurements, a fully calibrated model will give a faithful prediction of the instantaneous cylinder pressure. Construction of an inverse model has been approached in numerous ways including: i) by total appeal to the physics, ii) using semi-physical models; and by using physics-free functional approximation models such as artificial neural networks (ANNs). The use of purely physical dynamic models is generally a complex route that requires an understanding of all of the mechanics involved [7]. Inversion of such models throws up various problems including singular behaviour at specifically important crank angles such as TDC. Moreover owing to the importance of assigning the correct model parameter values generally suffers from modelling and calibration issues. The use of ANNs by contrast, requires no knowledge of the physics but the choice of architecture and training method are critical.

Whether physical or ANN models are used some pre-processing or filtering of measured data is often necessary to exclude responses that are not directly linked to cylinder pressure. Such non-immediate-cylinder-pressure-related responses can be embedded in both crank and block vibration measurements. Examples in crank responses include driveline torsional vibrations (which generally need to be removed by filtering in the frequency domain). Similarly, measured block vibration responses, may include the effect of events such as valve closures, injector actuation, and piston slap (which generally need to be removed by time-frequency analysis and filtering [8]). Suitably calibrated indirect reconstruction approaches used on nominally identical, but physically different (production) engines, may not immediately produce faithful predictions owing to small differences in materials, manufacture, and build [9]. To overcome this difficulty, methods must be capable of adaptation. The key challenge for any approach is to achieve high accuracy in

both peak pressure P_{max} and location of peak pressure θ_{max} on a multi-cylinder engine under transient conditions with cycle-to-cycle variability. Such conditions are more prominent for gasoline engines moving between part and low load. The more successful results reported have tended to be for diesel engines operating at full load. A crank kinematics approach for example [10] using a Radial Basis Function (RBF) Neural Network applied to a 4-cylinder diesel engine reconstructed P_{max} to within 5% and θ_{max} within $\pm 2^o$. Similarly in [11], using an RBF network applied to a 6 cylinder diesel data, accuracies were reported of P_{max} within 2.9% and θ_{max} with $\pm 1.5^o$. A Sliding-Mode Observer was used with diesel engine crank data [12], producing P_{max} within 2% and θ_{max} with $\pm 2^o$. The use of a physically-based torque model in [13], applied to a 2 l 4-cylinder diesel engine reported obtaining P_{max} within 2.3 to 11.3% and θ_{max} between -0.4^o and 4.4^o. The use of measured block and cylinder head vibration signals have also been successful on diesel engines in particular, the use of inverse filtering involving frequency response averaging and time-domain cepstral smoothing [14], applied to single cylinder diesel data, or the use of RBF network in [15] applied to 2-cylinder diesel data. Cyclo-stationary principles were exploited in [16] to reconstruct cylinder pressure from cylinder head bolt data taken from a 4 cylinder 2 stroke diesel engine to produce P_{max} within 10%. In [17] an auto-regressive-moving-average filter was applied to engine block acoustic emissions for a 10000 bhp slow-speed-marine diesel at ¼ load, and a small 4-stroke diesel engine to produce P_{max} within 7%. By contrast a Feed-forward ANN applied to cylinder head vibration data in [18] produced reconstruction for a 6 cylinder diesel engine of P_{max} within 2% and θ_{max} within $\pm 3.5^o$. And processing of block vibration using a Feed-Forward RBF network applied to a single-cylinder diesel in [19] reconstructed P_{max} within 2.7% and θ_{max} within $\pm 1.5^o$. Recursive estimation by applying a Kalman filter to 4-cylinder diesel engine structural vibration in [20] has recently been reported typically producing P_{max} within 6% and θ_{max} within 2.30°.

Turning attention to indirect reconstruction for gasoline engines, a second-order sliding mode differentiator for torque was combined in [21] with a single pressure measurement (from one cylinder) to obtain estimates of cylinder pressure for the other cylinders of a 4 cylinder DISI engine producing P_{max} within 5 – 10% and θ_{max} within $\pm 5^o$. An ANN was applied to crank kinematics in [22] obtained from a single-cylinder turbocharged SI engine to obtain P_{max} within 4 – 8%. Block vibrations, taken from a gasoline engine, have also been used in [23] to reconstruct using a time-varying transfer function to obtain P_{max} within 25% and a mean error in θ_{max} of 0.04^o and a standard deviation of 4.8^o. The use of data taken from a strain washer, fitted to head screws on 2-stroke SI engine and 4-stroke SI engines [24] shows generally good results using a linear prediction model results, which should be within 5% across a range of medium-high load operating conditions. And in [25] measurements of crank angle and crank speed (taken with a low resolution 72 ppr encoder) are related to cylinder pressure using an optimised Extreme Learning Machine model. Application of a recurrent (NARX) ANN, trained recurrently using an Extended Kalman Filter using high resolution crank encoder data taken from an I3 DISI engine in [26] showed successful reconstruction but training was extremely slow and the Network was prone to go unstable in a predictive mode (but then recover). An alternative fully-recurrent training method was applied in [27] to a NARX model using DISI engine crank data to produce at the same test point P_{max} within 10% and θ_{max} within $\pm 2^o$. At different test points, particularly at different speeds, predictions deteriorated. In a return to feed-forward ANN based prediction [28] used a delay-future predictions of cylinder pressure using both crank kinematics and block vibrations taken from a DISI engine. By careful pre-processing of measured data crank-based prediction accuracies were P_{max} within 3% and θ_{max} within $\pm 3^o$. Predictions using block vibration measurements were typically P_{max} within 10% and θ_{max} within $\pm 2^o$ (and better than using crank data).

Considerable recent interest has been placed on the use of in-cylinder pressure measurements to supply real-time model-based NO_X monitoring in diesel engines [29]. Related to this requirement is a technique for reconstructing cylinder pressure in multi-cylinder engines from a pressure sensor signal obtained from just one cylinder [30]. All of the methods that have been cited with quantified accuracy apply to data corresponding to steady-state engine conditions. The major problem area applies particularly to indirect cylinder pressure reconstruction for a gasoline engine operating under transient conditions in which the engine is made to sweep through a range of speeds particularly under low load conditions. In this paper, a new time-dependent nonlinear cylinder pressure reconstruction model is developed for use with measured gasoline engine crank kinematics operating either under steady-state or transient conditions. The objective of the paper is to develop the basis of this new method and to test its accuracy and efficiency, and to identify its potential suitability for adaptive reconstruction.

2. A TIME-DEPENDENT NONLINEAR INVERSE RECONSTRUCTION MODEL

Given that a direct model relating multi-cylinder engine pressure to crank kinematics is generally strongly nonlinear and cycle dependent [7], it is hypothesised that the inverse model is also strongly nonlinear and cycle dependent. Here, a nonlinear and cycle dependent model structure is proposed that allows the constituent nonlinear functional representations to be built-up adaptively. The model can then be calibrated using the standard tools of linear algebra.

2.1 The model structure

A time-domain prediction model to obtain the in-cylinder pressure $P_k(\theta(t))$ associated with Cylinder-*k* of a multi-cylinder engine is hypothesised to take the form:

$$P_k\big(\theta(t)\big) = F_1(\ddot{\theta}(t)) + F_2(\dot{\theta}(t)) + F_3(\dot{\theta}(t)) + F_4(\theta(t)) \qquad (1)$$

where $F_1()$ - $F_4()$ are four unknown (separable) nonlinear functions of the crank kinematics. In particular, F_1 is a function crank jerk $\dddot{\theta}(t_i)$, F_2 is a function of crank acceleration $\ddot{\theta}(t_i)$, F_3 is a function of crank velocity $\dot{\theta}(t_i)$, and F_4 is a function of crank displacement $\theta(t_i)$. Each of these kinematics are explicitly represented in the time-domain, namely as being explicit functions of time, rather than being specified in terms of crank angle values. The four unknown nonlinear functions $F_1()$ - $F_4()$ are each expanded into separate Chebychev Polynomials of the *First Kind* of degree m as follows:

$$\mathrm{F}_1(\dddot{\theta}(t)) = \sum_{j=0}^{m} \alpha_j(t)\, T_j(\dddot{\theta}(t)) \tag{2}$$

for crank jerk, and

$$\mathrm{F}_2(\ddot{\theta}(t)) = \sum_{j=0}^{m} \beta_j(t)\, T_j(\ddot{\theta}(t)) \tag{3}$$

for crank acceleration, and

$$\mathrm{F}_3(\dot{\theta}(t)) = \sum_{j=0}^{m} \gamma_j(t)\, T_j(\dot{\theta}(t)) \tag{4}$$

for crank velocity, and finally

$$\mathrm{F}_4(\theta(t)) = \sum_{j=0}^{m} \delta_j(t)\, T_j(\theta(t)) \tag{5}$$

for crank displacement, where in general $T_j(t)$ is a Chebychev polynomial of the *First Kind* of degree *j* which satisfies the condition: $T_0(t) = 1$, $T_2(t) = t$, and the recurrence relationship: $T_{j+1}(t) = 2tT_j(t) - T_{\mathrm{j\text{-}1}}(t)$. The set of 4*m* time-dependent model parameter functions: $\alpha_j(t)$, $\beta_j(t)$, $\gamma_j(t)$, and $\delta_j(t)$ are fitted using measured engine data.

Calibrating time dependent model equation (1) therefore makes use of measured samples of both the kinematics and cylinder pressure. And when the model has been calibrated, predictions of cylinder pressure $P_k(\theta(t))$ are based on instantaneous values of measured crank kinematics only. To ensure the full benefits of the Chebychev polynomials are realised, the kinematics $\dddot{\theta}(t_i)$, $\ddot{\theta}(t_i)$, $\dot{\theta}(t_i)$, $\theta(t_i)$, are separately scaled, by finding the maximum and minimum values of the entire calibration set for each kinematic, such that these extrema are effectively scaled to [-1,1]. The set of 4 derived scaling laws are then retained for use with all the subsequent test data.

2.2 Fitting the model

Since $T_0(t) = 1$ the coefficient associated with the first term in each of the functions F_1 - F_4 can, be absorbed, for example, into a single coefficient associated with function F_1. In general, to fit the parameters functions: $\alpha_j(t)$, $\beta_j(t)$, $\gamma_j(t)$, and $\delta_j(t)$ in equation (1), i.e. at specific instantaneous value of time t_i, a minimum of 4*m*-3 independent sets of measured kinematics $\theta(t_i), \dot{\theta}(t_i)$, $\ddot{\theta}(t_i)$, $\dddot{\theta}(t_i)$, and pressures $P(t_i)$, are needed corresponding to *N* different cycles of measured data all at the same nominal (synchronized) time t_i. For specific instantaneous value of time t_i, N independent sets of cycles of data, can be used in equation (1) to generate a matrix equation in the form:

$$\begin{bmatrix} 1 & T_1(\dddot{\theta}(t_{i1})) & T_2(\dddot{\theta}(t_{i1})) & \dots & T_1(\ddot{\theta}(t_{i1})) & T_2(\ddot{\theta}(t_{i1})) & \dots & T_1(\dot{\theta}(t_{i1})) & T_2(\dot{\theta}(t_{i1})) & \dots & T_1(\theta(t_{i1})) & T_2(\theta(t_{i1})) & \dots \\ 1 & T_1(\dddot{\theta}(t_{i2})) & T_2(\dddot{\theta}(t_{i2})) & \dots & T_1(\ddot{\theta}(t_{i2})) & T_2(\ddot{\theta}(t_{i2})) & \dots & T_1(\dot{\theta}(t_{i2})) & T_2(\dot{\theta}(t_{i2})) & \dots & T_1(\theta(t_{i2})) & T_2(\theta(t_{i2})) & \dots \\ \vdots & \vdots & \vdots & \vdots & \vdots & \vdots & \vdots & \vdots & \vdots & \vdots & \vdots & \vdots & \vdots \\ 1 & T_1(\dddot{\theta}(t_{iN})) & T_2(\dddot{\theta}(t_{iN})) & \dots & T_1(\ddot{\theta}(t_{iN})) & T_2(\ddot{\theta}(t_{iN})) & \dots & T_1(\dot{\theta}(t_{iN})) & T_2(\dot{\theta}(t_{iN})) & \dots & T_1(\theta(t_{iN})) & T_2(\theta(t_{iN})) & \dots \end{bmatrix} \begin{bmatrix} \alpha_0(t_i) \\ \alpha_1(t_i) \\ \alpha_2(t_i) \\ \vdots \\ \beta_1(t_i) \\ \beta_2(t_i) \\ \vdots \\ \gamma_1(t_i) \\ \gamma_2(t_i) \\ \vdots \\ \delta_1(t_i) \\ \delta_2(t_i) \\ \vdots \end{bmatrix} = \begin{bmatrix} P_k(t_{i1}) \\ P_k(t_{i2}) \\ \vdots \\ P_k(t_{iN}) \end{bmatrix}$$

… (6)

If N > 4m-3 independent sets of data are used, then equation (6) represents an oversubscribed system of dimension N x (4*m*-3) for which a least-square-error solution can be obtained by solving the (overdetermined) system of equations. In principle, a least-square solution to equation (6) can easily be obtained as a standard solution of the normal equation.

However by adopting the expansions precisely of the form equations (2) – (5), there is in practice a subtle built-in degeneracy in the system of equations (6) which becomes clear when the cycle-by-cycle variability in the $P(t_i)$ vector tends to zero. In this case $P(t_i)$ tends to a vector with identical components of magnitude *p*. This can be shown by considering the special case of an overdetermined system of equations $A\boldsymbol{y}=\boldsymbol{b}$, where A is any *n* x *m*

matrix of rank *m* (*m* <= *n*), but where vector **b** = c x column *j* of matrix A, (c being any real scalar), it is then not difficult to show that the solution vector is **y** = [0 0 … c … 0 0]$^{\mathrm{T}}$, where the nonzero value c is located on row *j* of **y**. The implications of this for the system equation (6), is that when variability in $P(t_i)$ is small, this is effectively where vector **b** is precisely p x column-1 of matrix A. The solution vector then gives $\alpha_0(t) = p$, and zero for all the other parameters. Unfortunately, even when there is significant cycle-by-cycle variability, this sensitivity prevails such that the rank of the system equations (6) is frequently < 4m-3 preventing a complete solution. To totally avoid this sensitivity the remedy is to remove the $\alpha_0(t)$ function entirely from the model by adopting a reduced system in the form:

$$\begin{bmatrix} T_1(\ddot{\theta}(t_{i1})) & T_2(\ddot{\theta}(t_{i1})) & \dots & T_1(\ddot{\theta}(t_{i1})) & T_2(\ddot{\theta}(t_{i1})) & \dots & T_1(\dot{\theta}(t_{i1})) & T_2(\dot{\theta}(t_{i1})) & \dots & T_1(\theta(t_{i1})) & T_2(\theta(t_{i1})) & \dots \\ T_1(\ddot{\theta}(t_{i2})) & T_2(\ddot{\theta}(t_{i2})) & \dots & T_1(\ddot{\theta}(t_{i2})) & T_2(\ddot{\theta}(t_{i2})) & \dots & T_1(\dot{\theta}(t_{i2})) & T_2(\dot{\theta}(t_{i2})) & \dots & T_1(\theta(t_{i2})) & T_2(\theta(t_{i2})) & \dots \\ \vdots & \vdots & \vdots & \vdots & \vdots & \vdots & \vdots & \vdots & \vdots & \vdots & \vdots & \vdots \\ T_1(\ddot{\theta}(t_{\mathrm{iN}})) & T_2(\ddot{\theta}(t_{\mathrm{iN}})) & \dots & T_1(\ddot{\theta}(t_{\mathrm{iN}})) & T_2(\ddot{\theta}(t_{\mathrm{iN}})) & \dots & T_1(\dot{\theta}(t_{\mathrm{iN}})) & T_2(\dot{\theta}(t_{\mathrm{iN}})) & \dots & T_1(\theta(t_{\mathrm{iN}})) & T_2(\theta(t_{\mathrm{iN}})) & \dots \end{bmatrix} \begin{bmatrix} \alpha_1(t_i) \\ \alpha_2(t_i) \\ \vdots \\ \beta_1(t_i) \\ \beta_2(t_i) \\ \vdots \\ \gamma_1(t_i) \\ \gamma_2(t_i) \\ \vdots \\ \delta_1(t_i) \\ \delta_2(t_i) \\ \vdots \end{bmatrix} = \begin{bmatrix} P_k(t_{i1}) \\ P_k(t_{i2}) \\ \vdots \\ P_k(t_{\mathrm{iN}}) \end{bmatrix}$$

… (7)

Again by writing the system of equations (7) in the form ***Ay*=*b*,** if the number of linear equations is chosen to be precisely N = 4m, then a unique solution ***y*** at each instant of time provides the set of 4m unknown parameters. If the number of system equations in (7) is chosen to be N > 4m, then again, at each instant of time, the system is overdetermined, and a standard least square solution can be used to obtain the 4m unknown parameters in ***y***, i.e.:

$$\boldsymbol{y} = (\mathrm{A}^{\mathrm{T}}\mathrm{A})^{-1}\mathrm{A}^{\mathrm{T}}\boldsymbol{b} \qquad (8)$$

The solution vector ***y*** can be readily obtained, for example, using the Matlab *'mldivide'* operator (i.e. the 'left matrix divide' or 'Backslash' operator).

3.0 THE ENGINE TEST FACILITIES AND DATA ACQUISITION DETAILS

Measured engine data used to test the model was obtained from an inline naturally-aspirated 3-cylinder 4-stroke direct-injected spark ignition gasoline engine located in a test cell and connected to a 130 kW McClure-type DC dynamometer rated at 130 kW/7000 rpm with maximum motoring power at 100 kW, and mounted in a rotating frame. There was no clutch used because the dynamometer was directly connected to the flywheel via a compliant torsional coupling as shown in figure 1. The critical torsional frequencies of the coupling shaft were fully known from the available data, namely the dynamometer armature inertia = 0.87 kgm^2, the flywheel Inertia = 0.12021 kgm^2, the crankshaft primary inertia = 0.02579 kgm^2, and the torsional stiffness = 1260 Nm/rad. The fundamental torsional frequency of the engine-dynamometer systems was 16.5 Hz which corresponded to a critical engine speed of 660 rpm. For data collection purposes this speed was avoided. Torque measurements were taken by a load cell on a moment arm on the dynamometer. The engine had 4 valves per cylinder and belt driven camshafts. The crank arrangement was such that successive firings are spaced by 240 CA˚ eliminating any combustion overlap. The engine bore = 79.0 mm, the stroke = 76.5 mm, and was fitted with EGR, knock control, and a torsional vibration damper. The swept volume = 1125 cc, compression ratio = 11.5.

Cylinder pressure measurements were obtained in each cylinder using Kistler type 6117BCD36 spark-plug mounted pressure sensors connected to Kistler type 5044 charge amplifiers to give via low noise charge cables, an operational range of 0 to 150 bar. Crank angle was measured with a high resolution (TDC-marked), nose-mounted 360 pulse Kistler type 2614A1 optical encoder. To prevent corruption of the crank kinematic signal by engine vibration, this was securely fixed to the cylinder block. By passing the encoder signal through a Kistler type 2614A4 pulse multiplier two output signals are produced. The first of these outputs is a single pulse for each rotation that was used as the TDC marker

by aligning the rising edge of the TTL signal. The second output produces either 360 pulses or 3600 pulses for each rotation, where the first pulse corresponds to TDC. This is because the encoder is capable of producing 3600 pulses per revolution by extrapolating the 360 genuinely physical pulses per revolution. Crank speed, crank acceleration, and crank jerk, are obtained by differentiating crank angle in the time domain, plus signal processing, and necessary corrections as explained in detail in Section 4.

Data Acquisition System

Accurate synchronous measurements of cylinder pressure and crank angle, was achieved using a dedicated National Instruments data acquisition system. This comprised an NI PXI-1031 chassis and a NI PXI-8331 interface with a Windows PC containing two input modules: the NI PXI-6133 analogue input module, and an NI PXI-6602 counter module (used as a timer). A total of 8 channels of data (with 14-bit synchronous sampling) were captured on the NI PXI-6133 analogue input module. Low noise co-axial cables were connected to the analogue inputs via a TB-2709 terminal block. This had a maximum input amplitude of 10V, and a maximum sampling rate of 2.5 MHz. The NI PXI-6133 module high dynamic range and high sampling rate rendered it particularly suited to the required application which, apart from the crankshaft encoder TTL signal output, was used to acquire data from other inputs. Crank encoder signal capture was achieved with 32-bit resolution via the NI PXI-6602 counter module with a maximum source frequency of 80 MHz with the signal transmitted into a BNC-2121 terminal block via low noise co-axial cables. Pegging of the cylinder pressure signals, details of the data acquisition rates, and noise suppression measures have been comprehensively described in [6].

Most combustion analysis systems acquire data at equal-spaced crank angles (i.e. in crank domain). Crank domain signal processing is not however adequate for the proposed application as the sampling frequencies then vary with engine speed, moreover there are limited options for aliasing protection which would undermine the fidelity of low frequency

data. Inverse cylinder pressure reconstruction models are therefore more appropriately calibrated (or trained in the case of machine learning) using time-domain rather than crank-angle domain data. Time-based data acquisition also removes the need for re-sampling. Synchronisation between the analogue inputs and the crank encoder TTL signal using time domain sampling was achieved by using the TDC pulse from the encoder to trigger the acquisition of all inputs for each cycle. This strategy also removes the problem of acquisition data drift which could potentially accumulate over a number of cycles.

Two significant issues relating to the data acquisition hardware are: i) the management of errors associated with the crank encoder, and ii) the treatment of the non-physically derived 0.1˚ resolution of the Kistler encoder. Regarding the encoder issue and the need for calibration, this is described in [26][27], and again in context in Section 4, but the successful resolution of the problem is described in detail in [6]. Essentially the problem stems from the fact that each of the 360 slits on the encoder disc are not precisely 1˚ owing to small random manufacturing errors. The encoder is a wholly acceptable way of measuring crank angle but numerical differentiation of the (cyclically-noisy) encoder crank angle signal to obtain velocity (and subsequently acceleration) is very sensitive to the manufacturing errors. The problem is largely solved by calibration [6] allowing a smooth crank angle signal to be obtained which can be differentiated to obtain crank velocity, acceleration, and jerk.

Regarding the second encoder issue, namely the non-physical 0.1˚ resolution from the 3600 ppr encoder, this stems from the encoder extrapolating data forward using two previous positions (assuming little change). Consequently, since the 0.1˚ is not a genuine physical measurement, the nominal high resolution signal was not used.

4.0 PROCESSING CYLINDER PRESSURE AND CRANK KINEMATIC DATA

Crank displacement is obtained as a function of time by re-sampling the 80 MHz counter intervals into constant time steps synchronised with the 2.5 MHz sampled cylinder pressure data. Several important signal processing operations are needed to prepare measured crank data obtained from the shaft encoder for use in model fitting and subsequent prediction of cylinder pressure. These include: i) a correction process to address small defects in the manufactured encoder disc, ii) finite difference operations to estimate derivatives, iii) band-pass filtering of acceleration data, iv) a cylinder pressure windowing operation, and v) the adoption of a prediction criterion to exclude unacceptable kinematics histories in the unseen crank data.

The first of these signal processing activities concerns removal of random manufacturing errors in the crank angle increments associated with the TTL signals measured by a production crank encoder. A correction procedure needed to overcome this problem is fully described in [6]. This procedure removes most of the errors associated with any manufacturing deficiencies. The resulting smooth signals are differentiated using finite differences to obtain for example, crank acceleration from crank velocity, and crank jerk $\dddot{\theta}(t_i)$ from crank acceleration. The standard central difference used is as follows:

$$\ddot{\theta}(t_i) = \frac{\dot{\theta}(t_{i+1}) - \dot{\theta}(t_{i-1})}{t_{i+1} - t_{i-1}} \tag{9}$$

The step in obtaining crank acceleration from crank velocity is affected by the limitations of encoder correction process that cannot entirely remove all the effects of the manufacturing errors. The result is that low-level noise on the crank velocity signal remains, is seriously exacerbated by the differentiation process needed to obtain crank acceleration. The noise that then appears has to be removed by a low-pass filter before attempting further differentiation to obtain jerk. However, at some engine speeds, subharmonic responses

are also visible in the low-pass filtered crank acceleration, these low frequency harmonics also need to be removed because they are not readily related to cylinder pressure.

Overall then, crank acceleration signals need to be band-pass filtered. The cause of the noise at high frequency stems from necessary corrections made to encoder data to account for manufacturing errors and is fully explained in [6]. The cause of the 'noise' at low frequency will be shown to stem from driveline nonlinear subharmonic responses, also reported elsewhere [31][32][33]. This is because the test engine, though not fitted with a Dual Mass Flywheel, is fitted with a flexible coupling. Nonlinearity of the flexible coupling can produce unexpected torsional responses at certain frequencies. For example, at 1000 rpm 30 Nm torque, figure 2 shows the crank acceleration in the frequency domain. The dominant crank acceleration component is the $1\frac{1}{2}$-order at 25 Hz. There are no subharmonic responses below the engine speed at 16.66 Hz. Figure 3 shows the crank acceleration in the frequency domain at 1500 rpm, 30 Nm torque. The dominant frequency is again the $1\frac{1}{2}$-order at 37.5 Hz, with a much smaller response at the engine speed at 25 Hz. There is however a significantly larger response at half the $1\frac{1}{2}$-order frequency of 18.72 Hz. This is a Period-2 driveline subharmonic response caused by nonlinearity in the coupling. Figure 4 shows the engine crank acceleration at 3000 rpm, 66 Nm torque. Again the $1\frac{1}{2}$-order component at 75 Hz is dominant, but there is evidence now of a Period-3 driveline subharmonic response at around 25 Hz. The important issue is that these subharmonic responses are difficult to correlate *per se* with in-cylinder pressures and therefore should be removed. Bandpass filtering of the acceleration for the model fitting process is needed to remove these low and high frequency effects, easily achieved here in the frequency domain by setting harmonics to zero below the low-frequency cut-off frequency and above the high cut-off frequency. In practical situations using real engine data, this band-pass filtering may be more appropriately achieved using either analogue or

digital filtering. Figure 5 shows an example of the crank acceleration signal in the time domain corresponding to a steady-state test point at 1500 rpm, 30 Nm torque with, and without, band-pass filtering, where the low cutoff frequency is 25 Hz and the high cutoff frequency is 100 Hz. Figure 6 shows the acceleration signal in the time domain associated with transient speed data, with and without corresponding band-pass filtering (transient data is shown shortly in Figure 7 and is used for model calibration and testing).

The adoption of a time domain 'data window' for calibration is justified since it is evident that in any forward crank dynamic model only the cylinder pressure trace shortly after Top Dead Centre (TDC) has any significant influence on the variability of crank kinematics. In a corresponding inverse model it would be expected that the relationship between crank kinematics and cylinder pressure would be confined to a similar region, shortly after TDC. To focus only on this region, the use of a data window is adopted for both cylinder pressure and crank kinematics. No model fitting or prediction takes place outside of this window regions. All cycles used, only include information within the data window, defined as a fraction of the entire cycle after TDC. Typical data windows correspond to around 15% of the total 720 degrees after TDC.

The final data processing activity is to improve the accuracy of model predictions using unseen data by the adoption of a criterion to exclude predictions which are calculated (*a priori*) to produce a poor calibration data peak pressure prediction. The basis of the approach, applied for each cycle of test data (i.e. different from the calibration data), is to find a particular cycle of calibration data that can be deemed to have 'closest' kinematics to the test cycle in some sense. This is achieved in general by computing the minimum normalised square error between the kinematics of a particular test cycle and the entire set of calibration data cycles. For the calibration cycle with 'closest' kinematics, the *'calibration peak pressure error'* is computed i.e. the absolute (normalised) difference between the predicted calibration peak pressure (for the closest cycle) and the corresponding

measured calibration peak pressure. If this normalised difference exceeds a specified criterion, then prediction for that particular test cycle will be discarded. To be specific, to find the calibration cycle with 'closest' kinematics, the kinematic error components are first computed, for example, the normalised jerk error component defined as:

$$\epsilon_{\Delta\ddot{\theta}} = \frac{\left\{\int_{t_t}^{t_2}(\ddot{\theta}(t)_{cal(i)} - \ddot{\theta}(t)_{val})^2 \mathrm{dt}\right\}^{1/2}}{\left\{\int_{t_t}^{t_2}(\ddot{\theta}(t)_{val})^2 \mathrm{dt}\right\}^{1/2}} \quad \text{for all calibration cycles } i \tag{10}$$

Similar expressions can be used to obtain the other normalised error components, i.e. the crank acceleration error component $\epsilon_{\Delta\ddot{\theta}}$, the crank velocity component $\epsilon_{\Delta\dot{\theta}}$, and the crank displacement component $\epsilon_{\Delta\theta}$. The minimum of the total sum of individual normalised error components is then found i.e.:

$$\in_{Total} = \min\{c_1\epsilon_{\Delta\ddot{\theta}} + c_2\epsilon_{\Delta\ddot{\theta}} + c_3\epsilon_{\Delta\dot{\theta}} + c_4\epsilon_{\Delta\theta}\} \tag{11}$$

where c_1 to c_4 are coefficients that can be used to weight particular kinematics. For the closest calibration cycle, which corresponds to the minimum found from equation (11), the calibration peak pressure error $\in_{P_{max}}$ is computed (as a percentage) i.e.

$$\in_{P_{max}} = 100*\mathrm{abs}((\hat{p}_{max} - P_{measured})/P_{measured}) \tag{12}$$

where $\hat{p}_{max}$ is the peak pressure predicted using the calibrated model (Equation (1)) with the 'closest' calibration kinematics, and $P_{measured}$ is the corresponding measured (calibration data) peak pressure. If the magnitude of $\in_{P_{max}}$ exceeds a chosen criterion ΔP_{crit} i.e.:

$$\in_{P_{max}} > \Delta P_{crit} \tag{13}$$

then that particular test cycle prediction is discarded.

One obvious difficulty with finding the 'closest' kinematics as described is that the closest kinematic components may actually correspond to different calibration cycles. For example the 'closest' crank jerk component may correspond to a different calibration cycle from the 'closest' crank acceleration component. To explore the implications of this possibility, all combinations of kinematics in equation (11) have been examined by varying coefficients c_1

to c_4 (in combinations, taking values either 0 or 1). The empirical evidence is conclusive, namely that the closest kinematic components do indeed correspond to different calibration cycles. It is found however that the use of the jerk component alone dominates, and is by far the most effective kinematic component in selecting which test cycles to discard by setting $c_1 = 1$, and $c_2 = c_3 = c_4 = 0$, choosing for example a criterion ΔP_{crit} at 3%.

5. TESTING THE MODEL USING MEASURED ENGINE DATA

Before showing cylinder pressure results under transient engine operating conditions, a convergence study was undertaken using measured steady-state engine data to establish a suitable number of terms to include in Chebychev expansions in equation (1) for each of equations (2) – (5). To do this a set of 95 cycles of steady-state engine data was used to fit the model. The fitted model was then used to predict cylinder pressures associated with the different set of 95 cycles of steady-state engine data under the same conditions i.e. at an engine speed of 1500 rpm and a torque of 30 Nm. No use is yet made in this convergence study of the *'calibration peak pressure error'* given by Equation (12). The discrete time interval chosen was 0.1ms. The degree of the Chebychev polynomials for model fitting and the prediction process was successively increased (by the same amount for each of the functions F_1 – F_4 in equation (1)). For each Chebychev model degree, the percentage errors in the maximum pressure P_{max} and its crank angle location θ_{max} were examined.

Table 1 shows the results of the convergence study, where it is evident that as the Chebychev model degree in Equation (1) is increased, the magnitude of errors continue to reduce until the model fitting starts to become a problem above Chebychev degree of 4 . This is indicated by the right hand column of Table 1 where occasional rank deficiency in the least square solution of equation (7) occurs at particular time instances. The

conclusion therefore is that the best practical Chebychev model is degree 4 meaning that for each instant of time, 16 unknown parameter values need to be found.

Table 1. The fitting and prediction errors associated with both peak pressure and location of peak pressure as a function of the number of terms in the Chebychev polynomial expansions using 95 cycles of data for fitting and 95 different cycles for prediction. (For the fitting and test data: mean P_{max} (fitting) = 33.37 Bar; standard deviation P_{max} (fitting) = 3.99 bar; mean P_{max} (test) = 33.21 Bar; standard deviation P_{max} (test) = 3.99 Bar).

Degree of the Chebychev Polynomial expansions in the model	Standard Deviation of percentage fitting error in P_{max}.	Standard Deviation of percent prediction error in P_{max}.	Standard Deviation of fitting error in θ_{max} (location of P_{max}) degrees.	Standard Deviation of prediction error in θ_{max} (location of P_{max}) degrees.	Comment
1	6.4401	6.3816	3.1954	2.6244	Model fitting totally stable (4 unknowns)
2	5.0444	5.1348	2.1447	2.2598	Model fitting totally stable (8 unknowns)
3	4.7564	6.2202	1.8303	2.6439	Model fitting totally stable (12 unknowns)
4	4.7101	12.3230	1.8477	2.6295	Model fitting totally stable (16 unknowns)
5	4.2141	78.1923	1.9378	8.6719	Model fitting showing occasional rank deficiency; Rank =19 (20 unknowns)
6	4.1420	398.6436	2.0117	8.6783	Model fitting showing frequent rank deficiency; Rank =23 (24 unknowns)

5.1 Cylinder Pressure reconstruction for transient data

Two sets of transient data were used to test the ability of equation (1) to reconstruct cylinder pressure under transient conditions. Figure 7 a) and b) shows engine speed and corresponding cylinder pressures for 188 cycles of data used to fit the model. Figure 7 c) and d) show 188 cycles of different test data used to verify the models prediction capability

just using the corresponding kinematics. To confirm that there are significant differences between the fitting data and the test data, figures 7e) and 7f) show the corresponding differences between the fitting data and the test data**.** Here the speed is sweeping down from over 2000 rpm to 1000 rpm and back up over 2000 rpm. Predictions were made of the test data using a Chebychev model order = 4 for each of the 4 functions F_1 – F_4 in equation (1). Regarding the efficiency of predictions, using an Intel Core i5 PC, the Matlab computations to fit the model with 188 cycles took 1.54 seconds, and the predictions for the 188 transient test cycles (including computation of the *'calibration peak pressure error'* Equation (12)) took 2.68 seconds. Figure 8 shows all the fitted model parameters in equation (1) as a function of time shown in milliseconds after TDC, where the parameters are solved at discrete times with a discrete time interval of 0.1 ms. The time-dependent parameters: $\alpha_1(t)$, $\alpha_2(t)$, $\alpha_3(t)$ and $\alpha_4(t)$ in the function $F_1(\ddot{\theta}(t))$ are shown in the left hand column of the figure 8. The 2nd column in Figure 8 shows the model time-dependent parameters corresponding to $\beta_1(t)$ - $\beta_4(t)$ in F_2; the 3rd column, the parameters for F_3; and the 4th column, the parameters for F_4. Interestingly all of the parameters eventually tend to zero which is a desirable property.

The calibrated model Equation (1) is used hereafter in predictive mode applied to validation data. To improve the accuracy of selective predictions, the *'calibration peak pressure error'* Equation (12)) was computed for each of the 188 test cycles and is shown in figure 9. Also shown in figure 9 is the 3% criterion line, i.e. acceptability criterion ΔP_{crit}=3. A number of test cycles (particularly at low speed) fail this criterion. The predictions failing this criterion were deemed to be of low confidence and were therefore excluded. Figure 10 shows an example of a complete pressure trace prediction of validation data in which the comparison with measured data is particularly good. Figure 11 shows an example where the prediction of validation data compared with the measured data is less ggod. Figure 12 shows a typical sample of 4 zoomed-in pressure trace

predictions of validation data compared with measured data. Figure 13 shows predicted peak pressures for validation data including those discarded by the 'calibration peak pressure error' criterion Equation (13)) compared with the measured peaks. Figure 14 shows the predicted locations of peak pressures for validation data (also including those discarded by failing the 'calibration peak pressure error' criterion) again compared with measured locations of peak pressure. Figure 15 shows, for both fitting and predictions, the percentage errors in the peak pressure P_{max} and the corresponding locations θ_{max}.

5.2 Discussion of results

Figure 9 confirms that a significant fraction of the calibration peak pressures errors (obtained by using just the jerk history in Equation (11)) are failing the 3% criterion. Discarding predictions can successfully produce very accurate cylinder pressure reconstruction as shown by figure 10. Figure 11 shows a predicted trace compared with measured which is less good although even in this case the magnitude of peak pressure is good (the location is less good). The 4 zoomed-in samples in figure 12 are typical of the accepted test cycle predictions compared with measured traces. These varying engine speed results in figure 12 confirm that the nonlinear time-dependent model described by equation (1) is sufficiently flexible to be able to adapt to the needs of an inverse dynamic model suitable for fast cylinder pressure reconstruction. (The model was also extended to include both delay-time and preview data (such as adopted in [28]) but it actually reduced the accuracy of predictions). The use of the appropriately easy-to-compute calibration peak pressures errors tested against the 3% acceptability criterion, appears to be an effective way of retaining high confidence predictions. The use of this measure for example, resulted in around 50% of the 188 test cycles being discarded. However for most of the accepted predictions which satisfied the chosen criterion, the level of agreement with measurement is good. Figures 13 and 14, which respectively show the prediction of

P_{max} and θ_{max}, confirm that some of the discarded predictions have particularly large errors. Figure 15, by focusing on the percentage errors in P_{max} and θ_{max}, shows that the accepted test prediction errors are similar to the calibration errors. The prediction errors in P_{max} for the fitting data were around 9% whereas the predicted errors in P_{max} on different data using the exclusion criterion set at 3% were less than 6.5%. The fitting errors in θ_{max} were around 3.2^o, and for predictions of different data, were less than 2.67^o. These significantly lower errors for predictions involving data different from the fitting data (compared with the errors in predicting the fitting data) stem from the use of the *'calibration peak pressure error' and the* criterion ΔP_{crit}=3. This has the effect of excluding *a priori* any predictions with low confidence, therefore giving high confidence to retained predictionsThe prediction model Equation (1) has been calibrated to predict pressures traces for one particular cylinder by using measured crank kinematics and measured cylinder pressure traces corresponding to that particular cylinder. For multi-cylinder engines, to predict pressure traces for different cylinders, the calibration process is exactly the same except of course the measured cylinder pressure traces correspond to the particular cylinder of interest.

Regarding the computational efficiency in fitting the model, this is very straight-forward and is thousands of times faster than the alternatives such as artificial neural networks and would therefore be very suitable as an adaptive model to take account in real time such as accounted for significant changes in engine operating conditions. The computational efficiency of predictions (including that of the kinematic 'unfamiliarity' measure) is sufficiently fast to adapt to real-time applications. A single cycle prediction using Matlab (on a PC with an Intel i5 processor) took less than 14 ms which is less than the duration of a single cycle on a 4-stroke engine running at 6000 rpm.

6. CONCLUSIONS

A new crank kinematics based time-dependent nonlinear engine cylinder pressure reconstruction model has been proposed and tested on data taken from a direct injected gasoline engine on a dynamometer. The model adapts to the required degree of nonlinearity needed by exploiting the properties of Chebychev polynomials for which the optimum degree has been found to be 4. Crank kinematics associated with crank jerk, acceleration, velocity, and crank angle are all used. The use of an *a priori* 'calibration peak pressure error' (based only on the use of the jerk history component) allows confident predictions to be retained, and low confidence predictions to be discarded. The computational efficiency of the model makes it very appropriate for adaptive real-time cylinder pressure reconstruction under transient engine speed conditions.

Acknowledgements
Data collection occurred during EPSRC contract No. EP/E03246X/1 with support of JLR Powertrain Research & Technology, Jaguar Land Rover Viscount 2 (W11/8 Unit C2), Millburn Hill Road, Cannon Park, Coventry, CV4 7HS.

References

[1] Yoon P., Park S., Sunwoo M., Ohm I., Yoon K.J. (2000), Closed-loop control of spark advance and air-fuel ratio in SI engines using cylinder pressure. SAE Technical Paper 2000-01-0933.

[2] Müller R., Hart M., Krötz G., Eickhoff M., Truscott A., Noble A., Cavalloni C., Gnielka M. (2000), Combustion Pressure Based Engine Management System. SAE Technical Paper 2000-01-0928.

[3] Madan Kumar, Tielong Shen (2017) In-cylinder pressure-based air-fuel ratio control for lean burn operation mode of SI engines, Energy, 120,106-116.

[4] Willems F., (2018) Is Cylinder Pressure-Based Control Required to Meet Future HD Legislation? IFAC-Papers On Line Vol 51, Issue 31, Pages 111-118. (part of special issue: 5th IFAC Conference on Engine and Powertrain Control, Simulation and Modeling E-COSM 2018 Changchun, China).

[5] Eriksson L., Thomasson A., (2017) Cylinder state estimation from measured cylinder pressure traces - A Survey, IFAC-Papers On Line 50-1, 11029–11039, 20th IFAC World Congress, Toulouse.

[6] Bennett C., (2014) 'Reconstruction of Gasoline Engine In-Cylinder Pressures Using Recurrent Neural Networks', PhD Thesis, University of Sussex.

[7] Potenza R., (2006), Engine cylinder pressure reconstruction using neural networks and crank kinematics. Doctoral thesis, University of Sussex.

[8] Vulli S., Dunne J. F., Potenza R., Richardson D., King, P., (2009) Time-Frequency Analysis of Single-Point Engine-Block Vibration Measurements for Multiple Excitation-Event Identification. *Journal of Sound and Vibration*, 321, 1129-1143.

[9] Potenza R., Dunne, J. F., (2003) The effect of Variability on Engine Cylinder Pressure Reconstruction', 8th International Conference on Recent Advances in Structural Dynamics, ISVR, Southampton July 14-16th.

[10] Gu F., Jacob P.J., Ball A.D. (1999) Non-parametric models in the monitoring of engine performance and condition Part 2: Non-intrusive estimation of diesel engine cylinder pressure and its use in fault detection. Proceedings of the Institution of Mechanical Engineers Part D 1999, Vol 213(2) p135-143.

[11] Johnsson R., (2006), Cylinder pressure reconstruction based on complex radial basis function networks from vibration and speed signals. Mechanical Systems and Signal Processing Vol. 20 Issue 8 Nov. 2006 p1923-1940.

[12] Al-Durra A., Fiorentini L., Canova M., Yurkovich S., (2011), A model-based estimator of engine cylinder pressure imbalance for combustion feedback control applications. American Control Conference 2011 p991-996 ISSN:0743-1619.

[13] Liu F., Amaratunga A.J., Collings N., Soliman A., (2012), An experimental study on engine dynamics model based in-cylinder pressure estimation. SAE Technical Paper 2012-01-0896.

[14] Gao Y., Randall R.B., (1999), Reconstruction of diesel engine cylinder pressure using a time domain smoothing technique. Mechanical Systems and Signal Processing Vol.13, Issue 5 September 1999 p709-722.

[15] Du H., L Zhang L., Shi X., (2001), Reconstructing cylinder pressure from vibration signals based on radial basis function networks, Proceedings of the Institution of Mechanical Engineers Part D 2001. Vol. 215(6) p761-767.

[16] Antoni J., Daniere J., Guillet F., Randal R.B., (2002), Effective vibration analysis of IC engines using cyclostationarity Part ii} New results on the reconstruction of the cylinder pressures. Journal of Sound and Vibration Volume 257 Issue 5 November 2002, p839-856.

[17] El-Ghamry M., Steel J.A., Reuben R.L., Fog T.L., (2004), Indirect measurement of cylinder pressure from diesel engines using acoustic emission. Mechanical Systems and Signal Processing Vol.19, Issue 4 July 2005 p751-765.

[18] Yong X., Guiyou H., Chunrong S., Zhibing N., Wu Z., (2010), Reconstruction of cylinder pressure of I.C. engine based on neural networks. First International Conference on Pervasive Computing, Signal Processing and Applications, September 2010 p924-927.

[19] Bizon K., Continillo G., Mancaruso E., Vaglieco B.M., (2011), Reconstruction of in-cylinder pressure in a diesel engine from vibration signal using a RBF neural network model. SAE Technical Paper 2011-24-0161.

[20] Han R., Bohn C., Bauer G., (2018) Recursive Engine In-Cylinder Pressure Estimation Using Kalman Filter and Structural Vibration Signal IFAC-Papers On Line, Vol. 51, Issue 31, Pages 700-705. (part of special issue: 5th IFAC Conference on Engine and Powertrain Control, Simulation and Modeling E-COSM 2018 Changchun, China).

[21] Hamedovi H., Raichle F., Bohme J.F., (2005), In-cylinder pressure reconstruction for multi-cylinder SI engine by combined processing of engine speed and one cylinder pressure. IEEE International Conference on Acoustics, Speech and Signal Processing (ICASSP) March 2005, Proceedings Volume 5, p677-680.

[22] Taglialatela F., Lavorgna M., Mancaruso E., Vaglieco B.M., (2013), Determination of combustion parameters using engine crankshaft speed. Mechanical Systems and Signal Processing Vol. 38 Issue 2 p628-633.

[23] Villarino R., Böhme J.F., (2003), Fast in-cylinder pressure reconstruction from structure-borne sound using the EM algorithm. IEEE International Conference on Acoustics, Speech and Signal Processing (ICASSP) April 2003 Vol. 6 p597-600.

[24] Fiorini N., Romani L., Bellissima A., Vichi G., Bianchini A., Ferrara G., (2018). An indirect in-cylinder pressure measurement technique based on the estimation of the mechanical strength acting on an engine head screw: development and assessment, Energy Procedia, 695-702. (73rd Conference of the Italian Thermal Machines Engineering Association (ATI 2018), 12–14 Pisa).

[25] Mariani V. C., Och S. H., dos Santos Coelho L, and Dominguese E., (2019) Pressure prediction of a spark ignition single cylinder engine using optimized extreme learning machine models, Applied Energy 249, 204–221.

[26] Potenza R., Dunne J.F., Vulli S., Richardson D., King P., (2007), Multicylinder engine pressure reconstruction using NARX neural networks and crank kinematics. International Journal of Engine Research 2007 Vol. 8 No. 6 p499-518.

[27] Bennett C., Dunne J.F., Trimby S., Richardson D., (2017) 'Engine Cylinder Pressure Reconstruction using Crank Kinematics and Recurrently-Trained Neural Networks' *Journal of Mechanical Systems and Signal Processing.* 85, 126-145 (published on-line 18th August 2016).

[28] Trimby S., Dunne J.F., Bennett C., Richardson D., (2017) 'A unified approach to engine cylinder pressure reconstruction using time-delay neural networks with crank kinematics or block vibration measurements' IMechE *International Journal of Engine Research 18(3).*

[29] Cho H., Fulton B., Upadhyay D., Brewbaker T., van Nieuwstadt M., (2018), In-cylinder pressure sensor–based NO_x model for real-time application in diesel engines. *International Journal of Engine Research* Vol. 19 Issue 3. p293-307.

[30] Kulah S., Forrai A., Rentmeester F., Donkers T., Willems F., (2018), Robust cylinder pressure estimation in heavy-duty diesel engines. *International Journal of Engine Research* Vol. 19 Issue 2 p179-188.

[31] Kim, T.C., Rook, T.E., and Singh R., (2005) Super-and sub-harmonic response calculations for a torsional system with clearance nonlinearity using the harmonic balance method *Journal of Sound and Vibration*, 281, 965–993.

[32] Walter A., Murt M., Kiencke U., Jones S., and Winkler T. (2008) Compensation of sub-harmonic vibrations during engine idle by variable fuel injection control. Proceedings of the 17th World Congress IFAC, Seoul, Korea, July 6-11,

[33] Andersson N., Abrahamsson T. (2012) Driveline model calibration and validation in an automotive 4-cylinder Diesel application. Proceedings of ISMA2012-USD2012. KU-Leuvan.

LIST OF FIGURES

Figure 1. The engine test facility and instrumentation showing a 3-cylinder 4-stroke direct-injected spark ignition gasoline engine connected via a compliant torsional coupling to a 130 kW McClure-type DC dynamometer.

Figure 2. Crank acceleration in the frequency domain for an engine speed of 1000 rpm, 30 Nm torque, showing a dominant 1½-order component at 25 Hz but no subharmonic responses below the engine speed at 16.66 Hz.

Figure 3. Crank acceleration in the frequency domain for an engine speed of 1500 rpm, 30 Nm torque showing a dominant 1½-order component at 37.5 Hz, with a much smaller response at the engine speed at 25 Hz but with a significantly larger response at half the 1½-order frequency of 18.72 Hz.

Figure 4. Crank acceleration at 3000 rpm, 66 Nm torque showing the 1½-order component at 75 Hz is dominant, but evidence of a Period-3 driveline subharmonic response at around 25 Hz.

Figure 5. Crank acceleration signal in the time domain associated with steady-state engine speed of 1500 rpm, 30 Nm torque with and without band-pass filtering, where the low cutoff frequency is 25 Hz and the high cutoff frequency is 100 Hz.

Figure 6. Crank acceleration signal in the time domain associated with transient speed data ranging between 2200 and 800 rpm, with and without corresponding band-pass filtering, where the low cutoff frequency is 25 Hz and the high cutoff frequency is 100 Hz.

Figure 7. Crank speed and corresponding cylinder pressures. a) and b): 188 cycles of fitting data (crank angle, acceleration, and jerk data not shown); c) and d): 188 cycles of test data**;** e) and f) the corresponding differences between the fitting data and the test data.

Figure 8. The fitted model parameters in equation (1) as functions of time in milliseconds after TDC, shown at discrete times at intervals of 0.1 ms.

Figure 9. The 'calibration peak pressure error' (equation (12)) computed for 188 transient test cycles. Also shown is the 3% acceptability criterion i.e. ΔP_{crit}=3.

Figure 10. Cylinder pressure prediction trace as an example of a good validation: predicted trace '---', and its corresponding maximum '*'; the measured pressure trace: '.', and its corresponding maximum 'o'.

Figure 11. Cylinder pressure trace prediction as an example of a poor validation: predicted trace '---', and its corresponding maximum '*'; the measured pressure trace: '.' and its corresponding maximum 'o'.

Figure 12. A sample of validation pressure traces as a function of crank angle after TDC. Measured pressure traces '.'; corresponding locations of peak pressure 'o'; predicted pressure traces '- -'; corresponding locations of peak pressure '*'.

Figure 13. Peak pressures for validation data including those discarded by using the 'calibration peak pressure error' (equation (12)). Measured peak pressures, 'o', predicted peak pressures: '*', Measured peaks discarded using the'calibration peak pressure error': '•', the discarded predictions of peak pressure for validation data '•'.

Figure 14. Locations of peak pressures for validation data including those ignored by the 'calibration peak pressure error' (equation (12)). Measured locations of peak pressure, 'o', predicted locations of peak pressures: '*', Measured locations of peaks ignored using the'calibration peak pressure error': '•', the discarded predicted of the locations of peak pressure for validation data '•'.

Figure 15. Prediction errors associated with peak pressure P_{max} and its location θ_{max} for the model fitting data (left), and all the previously unseen data (right) for which the 'calibration peak pressure error' (equation (12)) is satisfying the 3% acceptability criterion ΔP_{crit}=3.

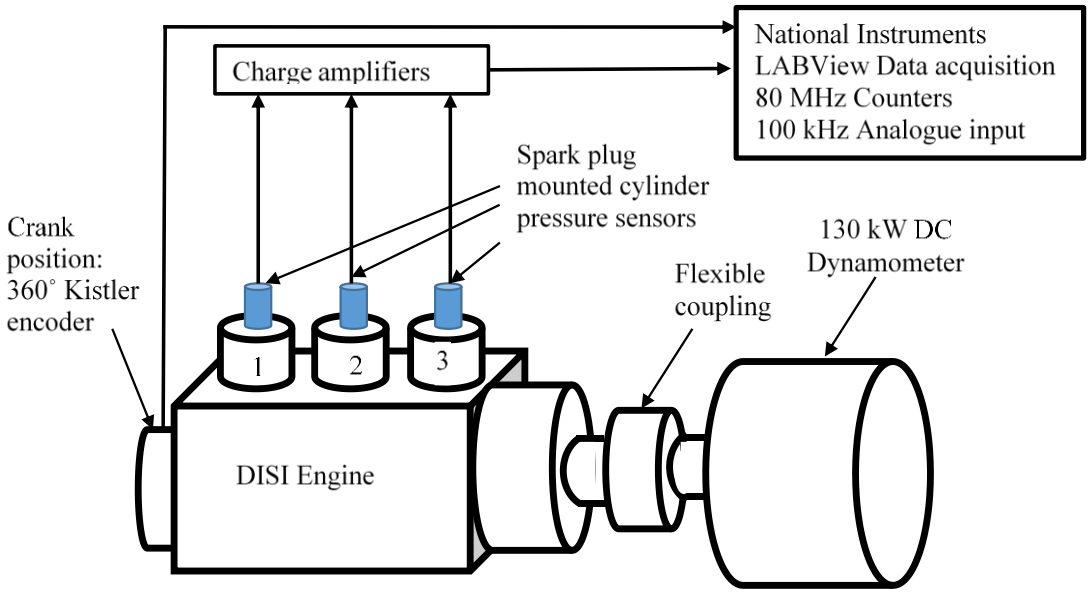

Figure 1. The engine test facility and instrumentation showing a 3-cylinder 4-stroke direct-injected spark ignition gasoline engine connected via a compliant torsional coupling to a 130 kW McClure-type DC dynamometer.

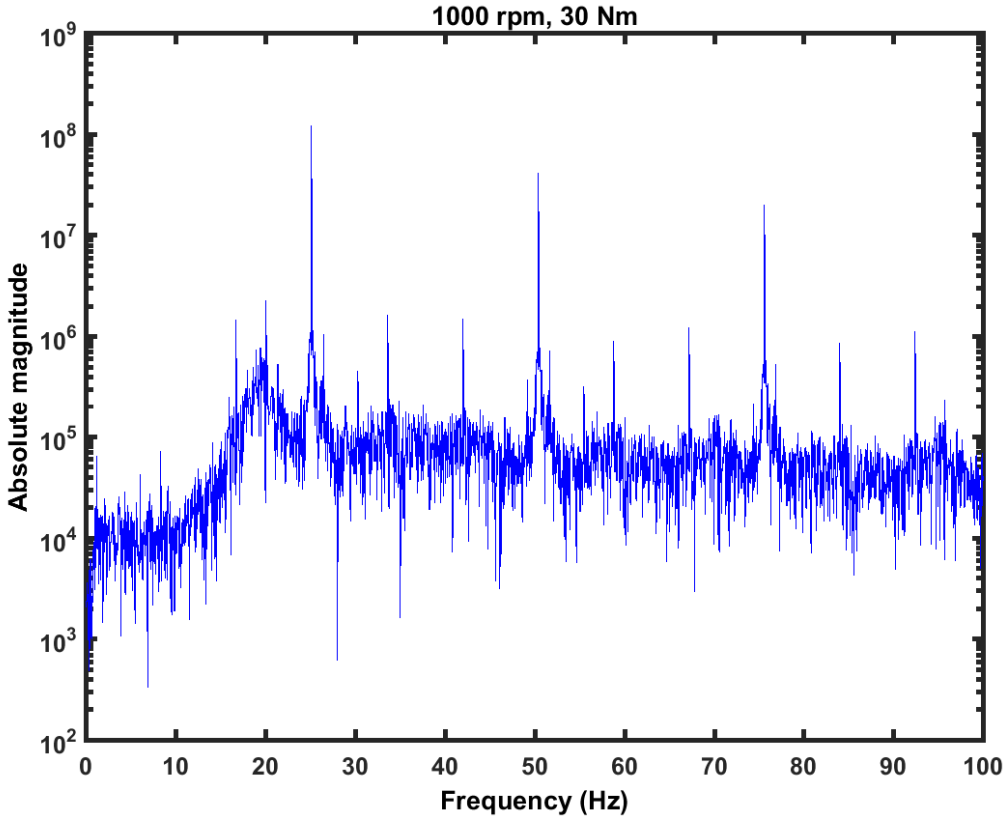

Figure 2. Crank acceleration in the frequency domain for an engine speed of 1000 rpm, 30 Nm torque, showing a dominant 1½-order component at 25 Hz but no subharmonic responses below the engine speed at 16.66 Hz.

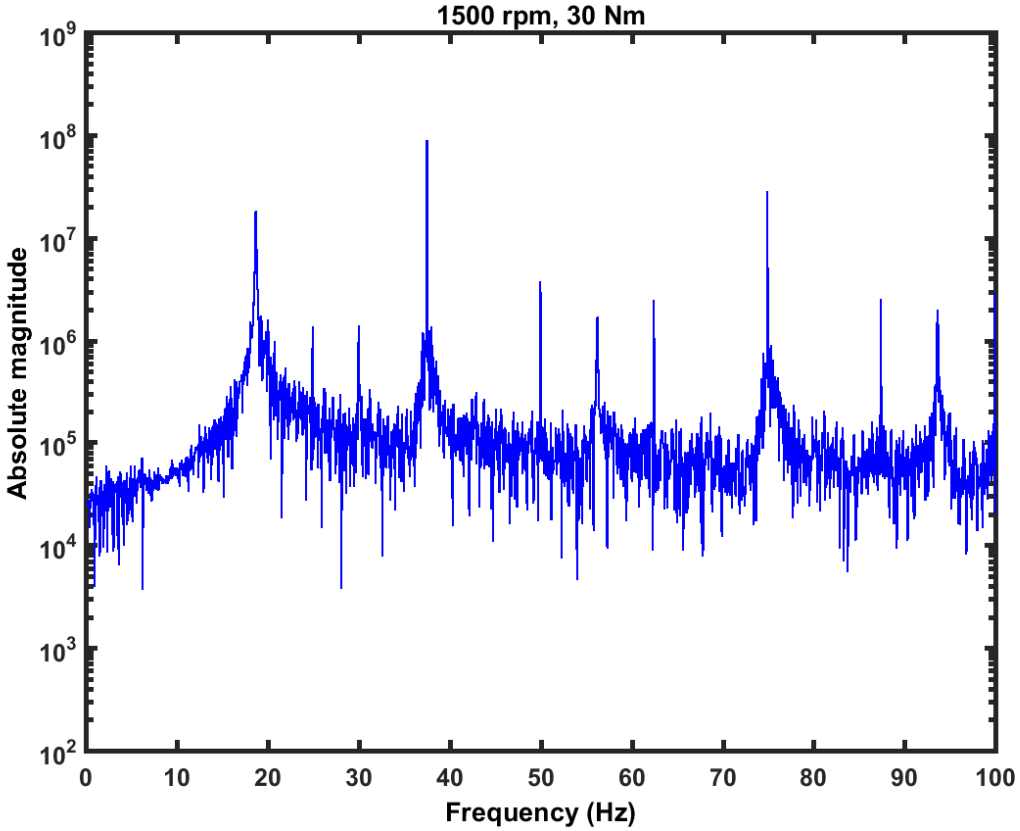

Figure 3. Crank acceleration in the frequency domain for an engine speed of 1500 rpm, 30 Nm torque showing a dominant 1½-order component at 37.5 Hz, with a much smaller response at the engine speed at 25 Hz but with a significantly larger response at half the 1½-order frequency of 18.72 Hz.

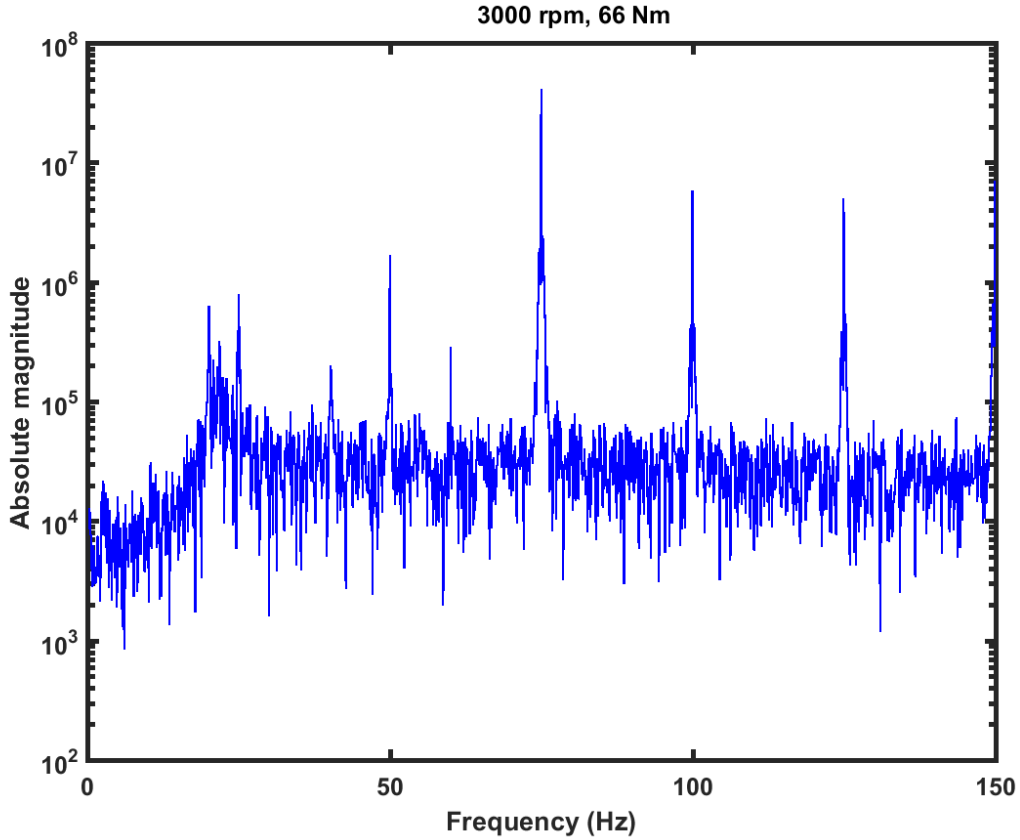

Figure 4. Crank acceleration at 3000 rpm, 66 Nm torque showing the 1½-order component at 75 Hz is dominant, but evidence of a Period-3 driveline subharmonic response at around 25 Hz.

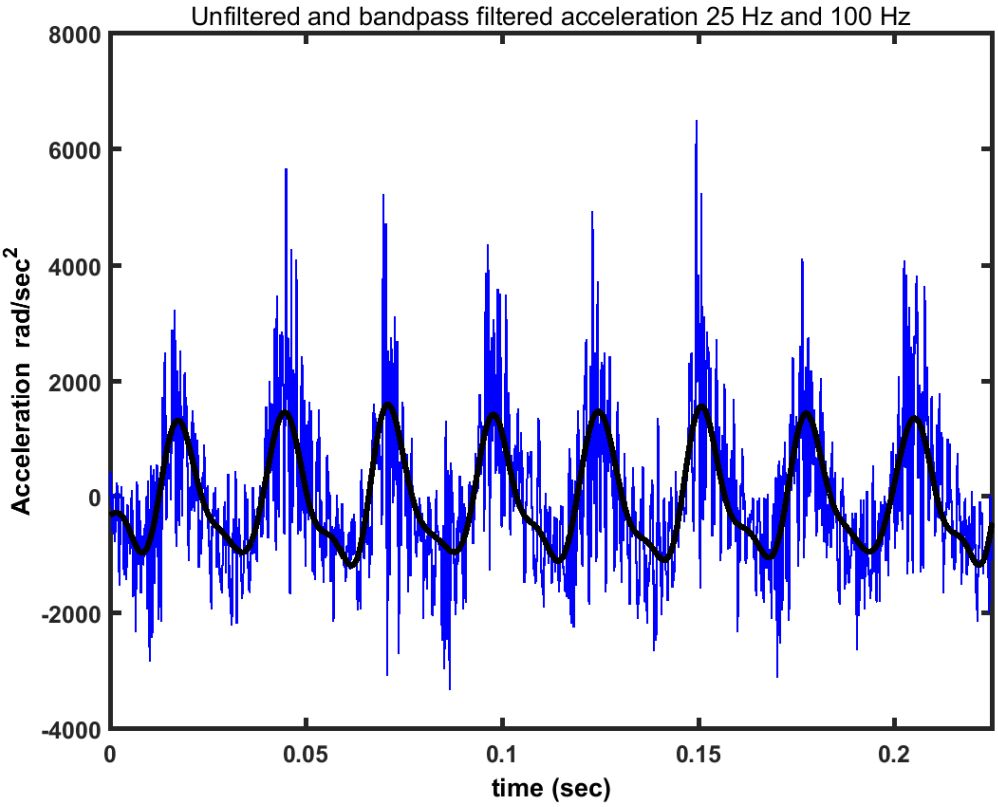

Figure 5. Crank acceleration signal in the time domain associated with steady-state engine speed of 1500 rpm, 30 Nm torque with and without band-pass filtering, where the low cutoff frequency is 25 Hz and the high cutoff frequency is 100 Hz.

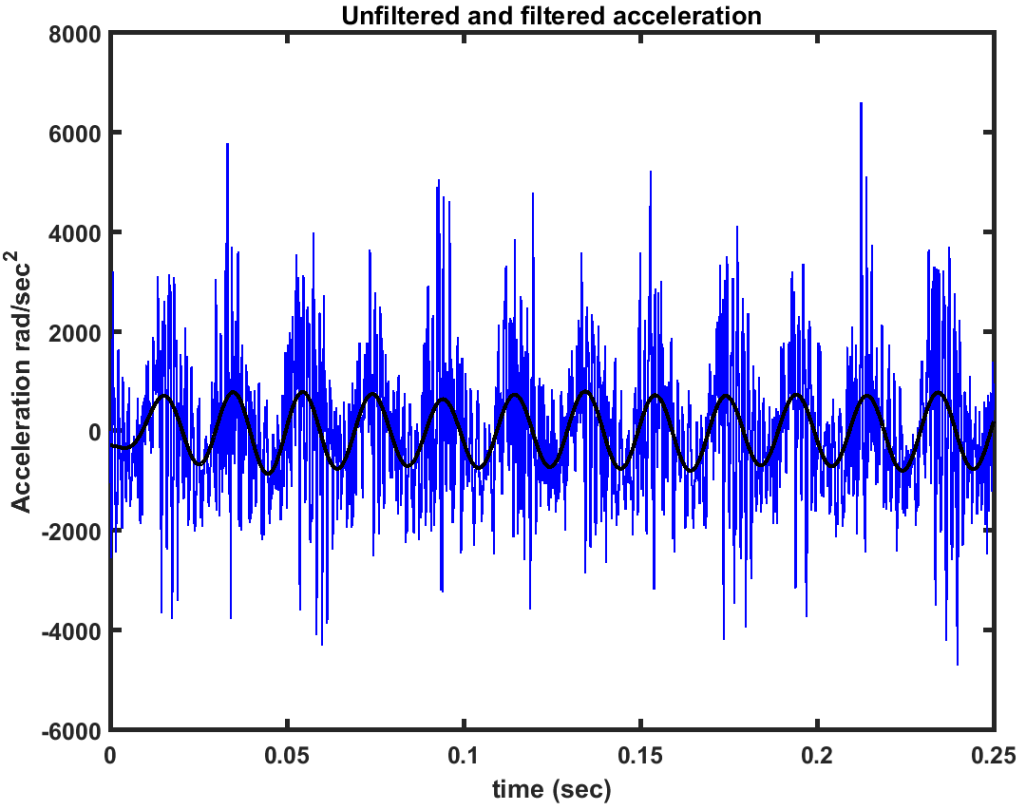

Figure 6. Crank acceleration signal in the time domain associated with transient speed data ranging between 2200 and 800 rpm, with and without corresponding band-pass filtering, where the low cutoff frequency is 25 Hz and the high cutoff frequency is 100 Hz.

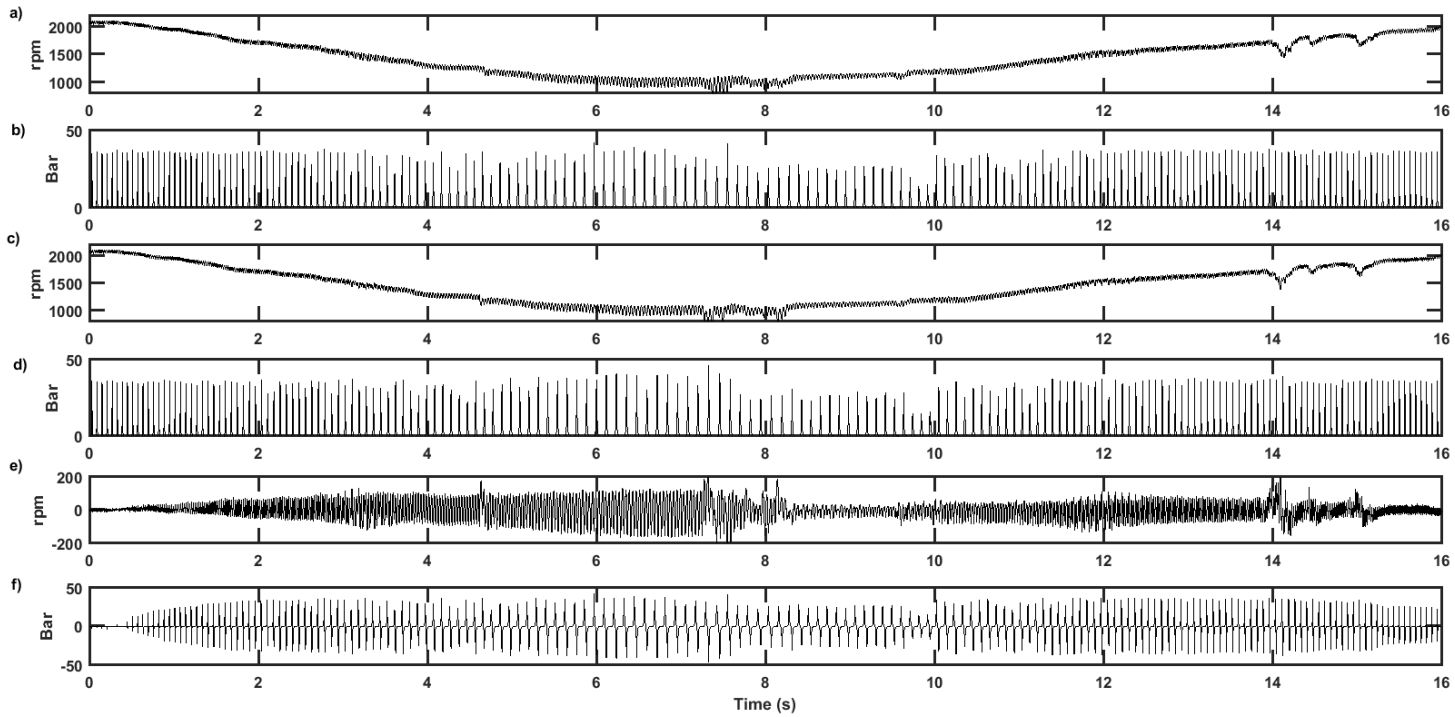

Figure 7. Crank speed and corresponding cylinder pressures. a) and b): 188 cycles of fitting data (crank angle, acceleration, and jerk data not shown); c) and d): 188 cycles of test data; e) and f) the corresponding differences between the fitting data and the test data.

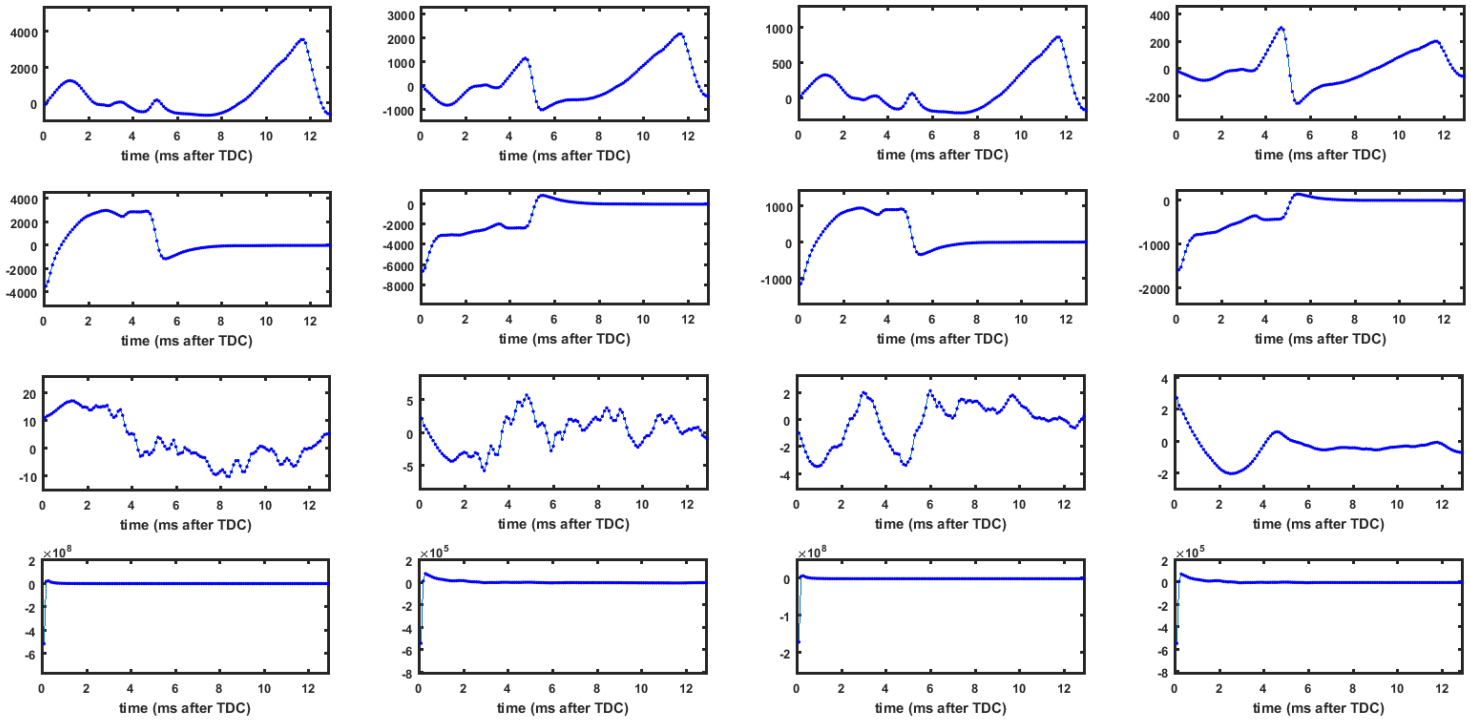

Figure 8. Fitted model parameters in equation (1) as functions of time in milliseconds after TDC, shown at discrete times intervals of 0.1 ms. Parameters $\alpha_1(t)$, $\alpha_2(t)$, $\alpha_3(t)$ and $\alpha_4(t)$ in the function $F_1(\ddot{\theta}(t))$ are shown in the left hand column; parameters $\beta_1(t)$ - $\beta_4(t)$ in the 2nd column; parameters for F_3 and F_4 are shown in the 3rd and 4th columns respectively.

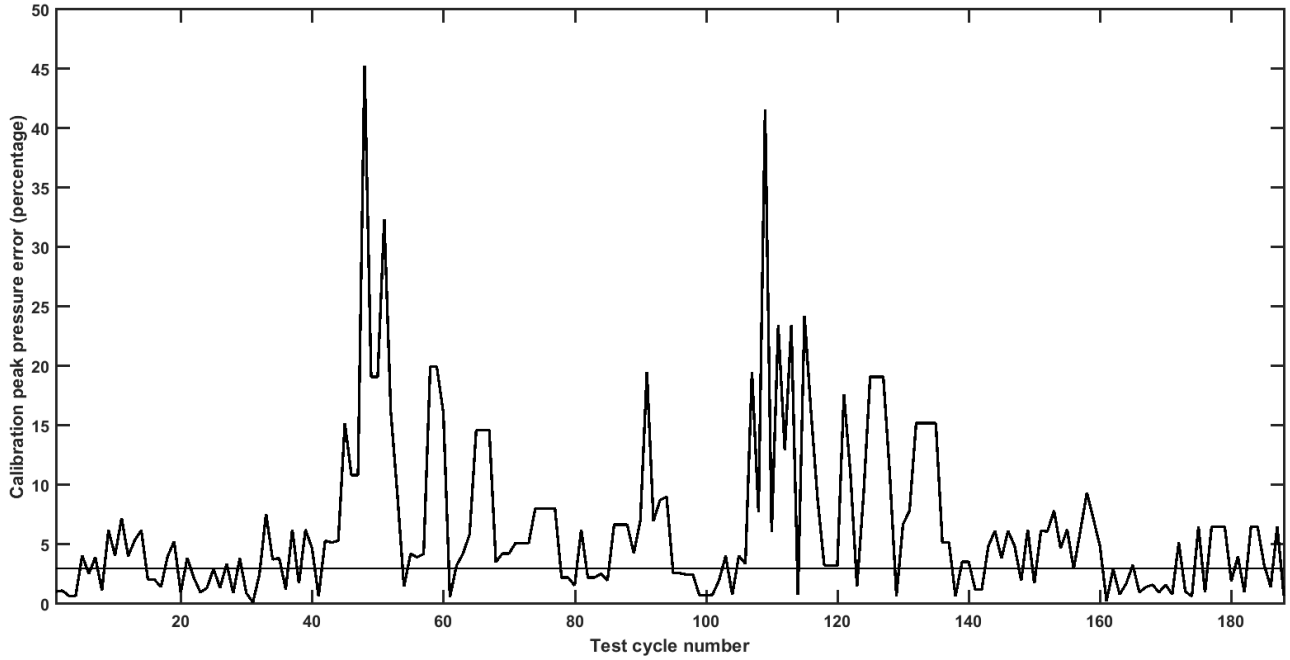

Figure 9. The 'calibration peak pressure error' (equation (12)) computed for 188 transient test cycles. Also shown is the 3% acceptability criterion i.e. ΔP_{crit}=3.

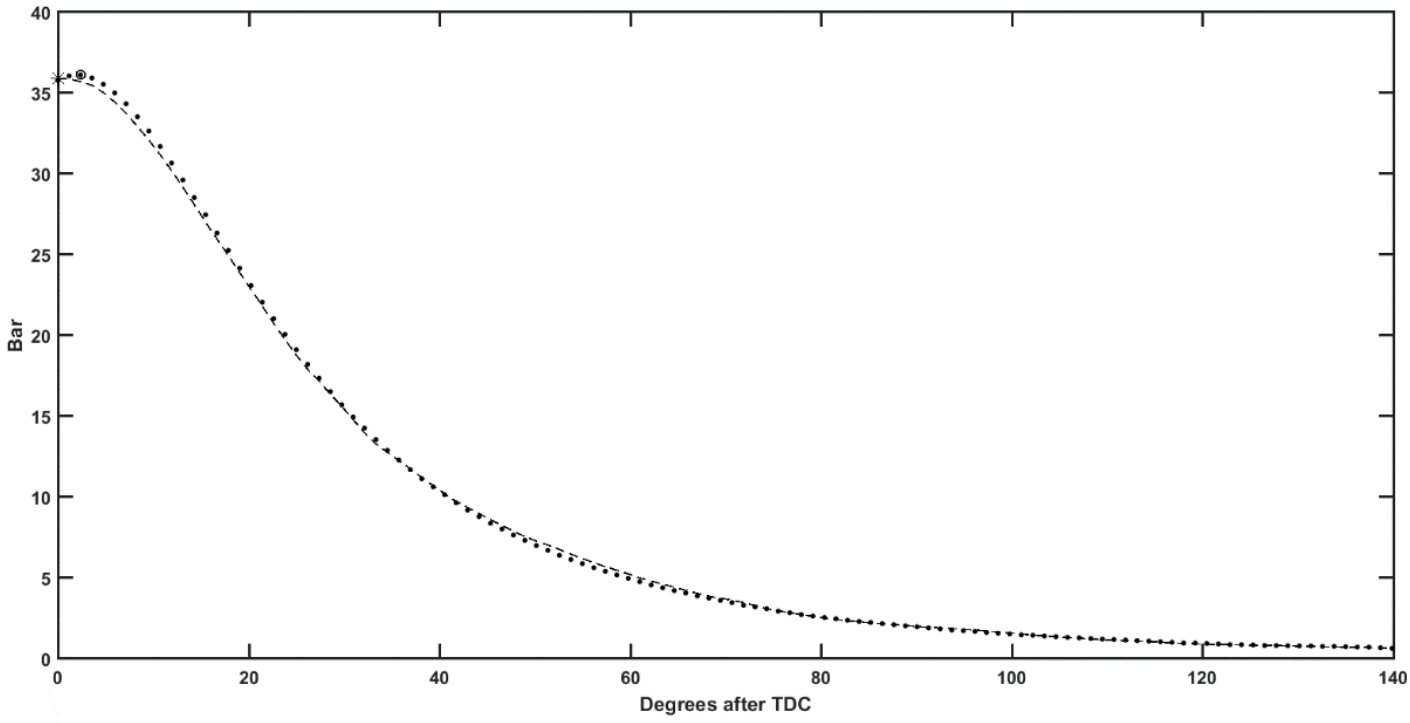

Figure 10. Cylinder pressure prediction trace as an example of a good validation: predicted trace '---', and its corresponding maximum '*'; the measured pressure trace: '.', and its corresponding maximum 'o'.

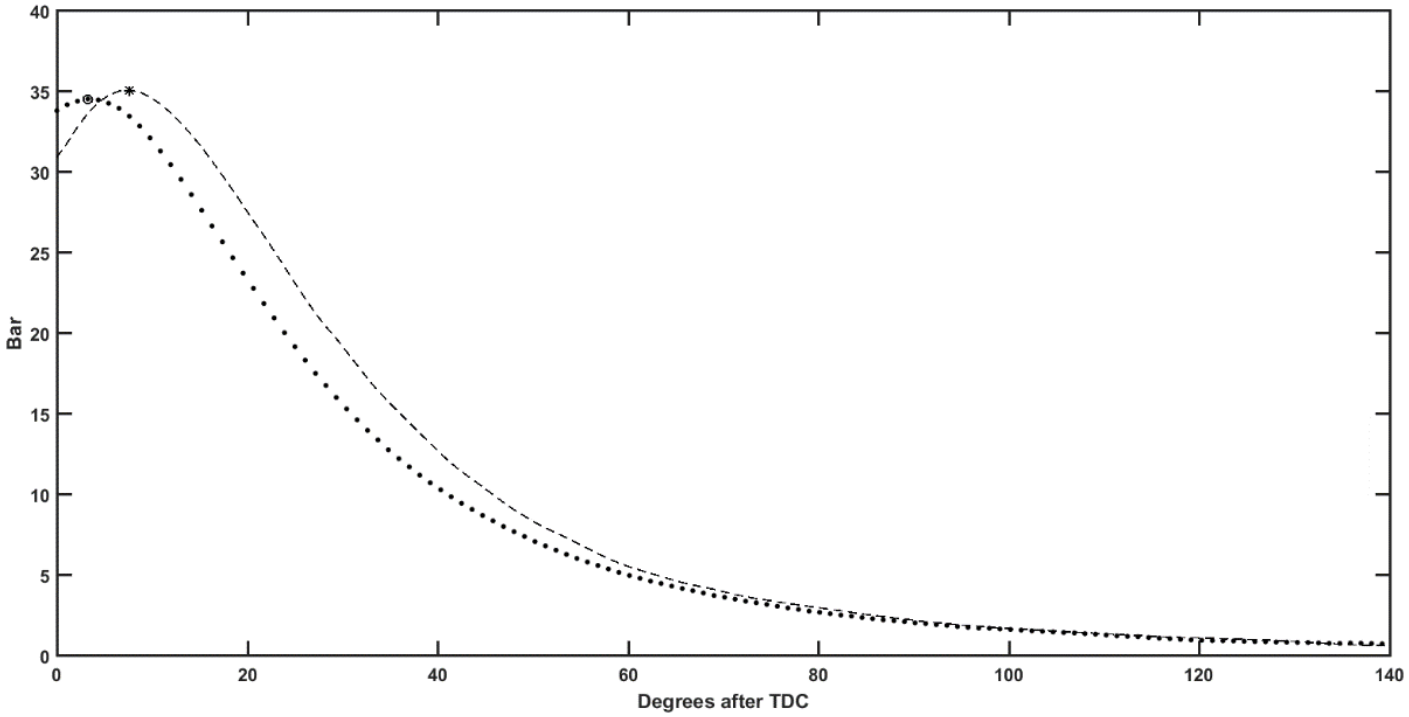

Figure 11. Cylinder pressure trace prediction as an example of a poor validation: predicted trace '---', and its corresponding maximum '*'; the measured pressure trace: '.' and its corresponding maximum 'o'.

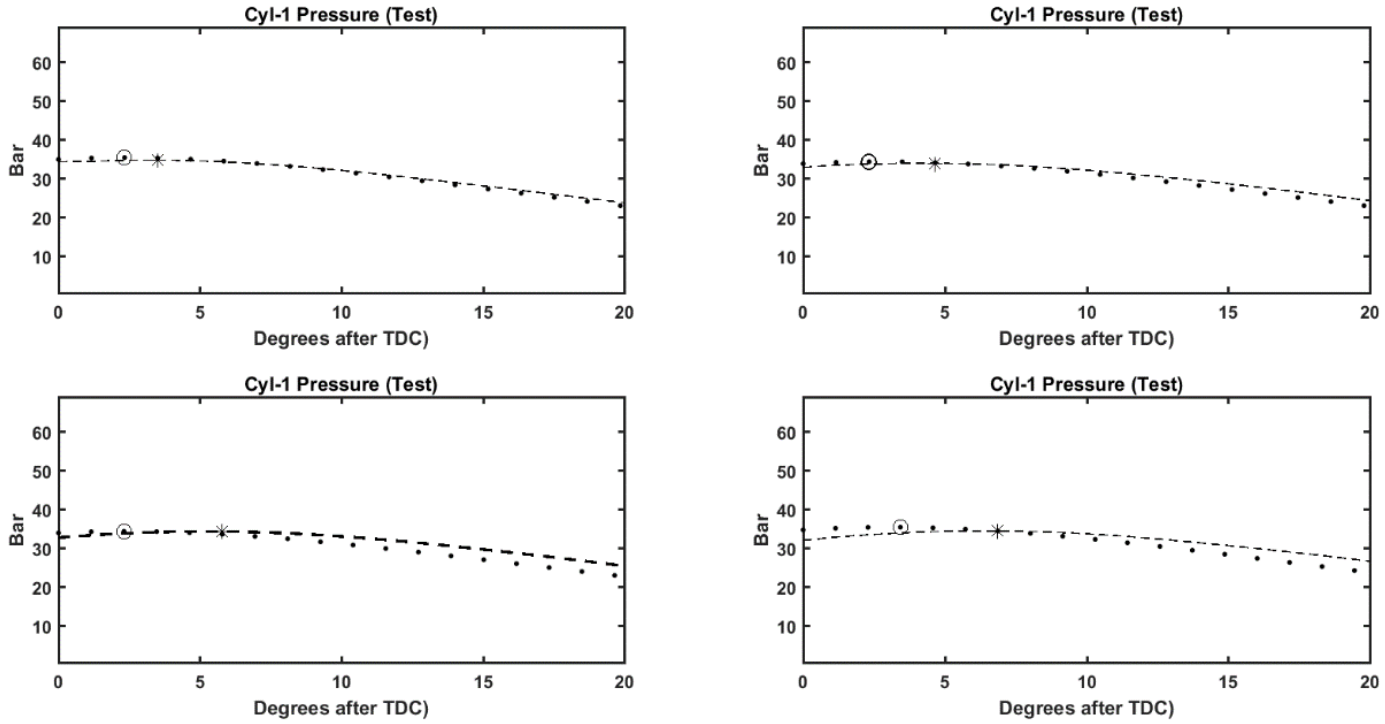

Figure 12. A sample of validation pressure traces as a function of crank angle after TDC. Measured pressure traces '.'; corresponding locations of peak pressure 'o'; predicted pressure traces '- -'; corresponding locations of peak pressure '*'.

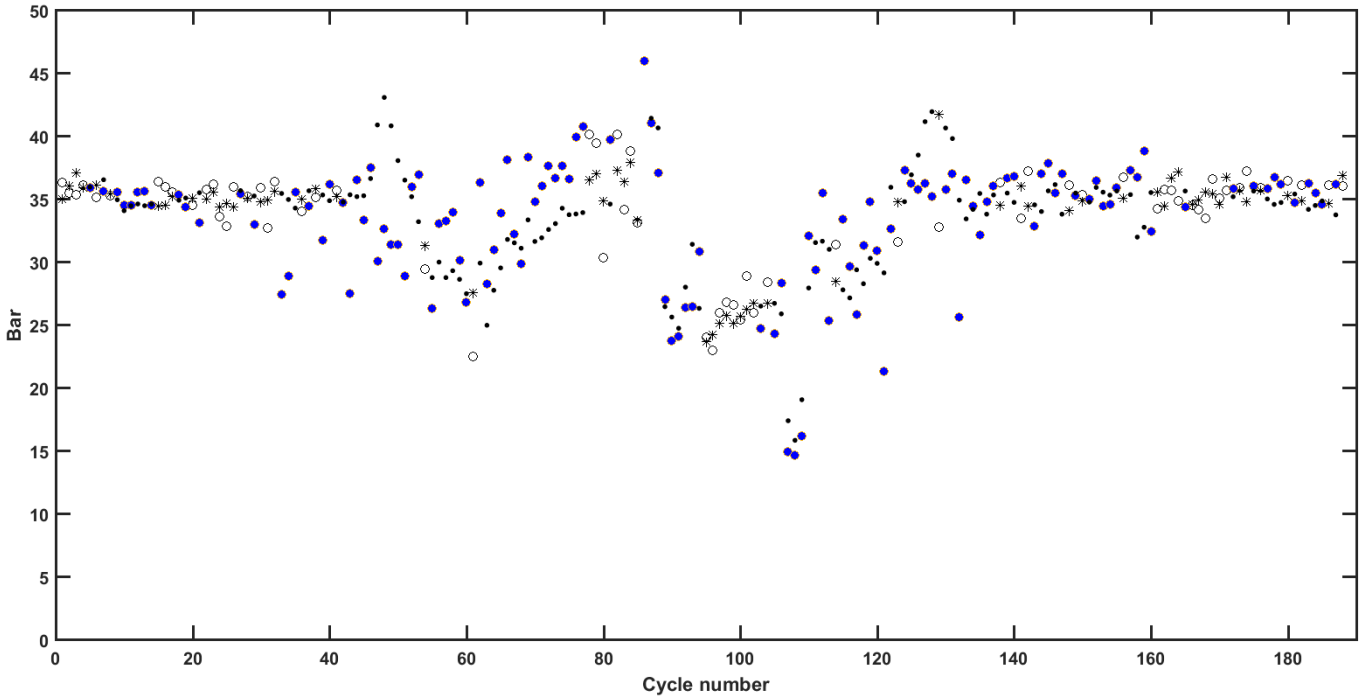

Figure 13. Peak pressures for validation data including those discarded by using the 'calibration peak pressure error' (equation (12)). Measured peak pressures, 'o', predicted peak pressures: '*', Measured peaks discarded using the'calibration peak pressure error': '•', the discarded predictions of peak pressure for validation data '•'.

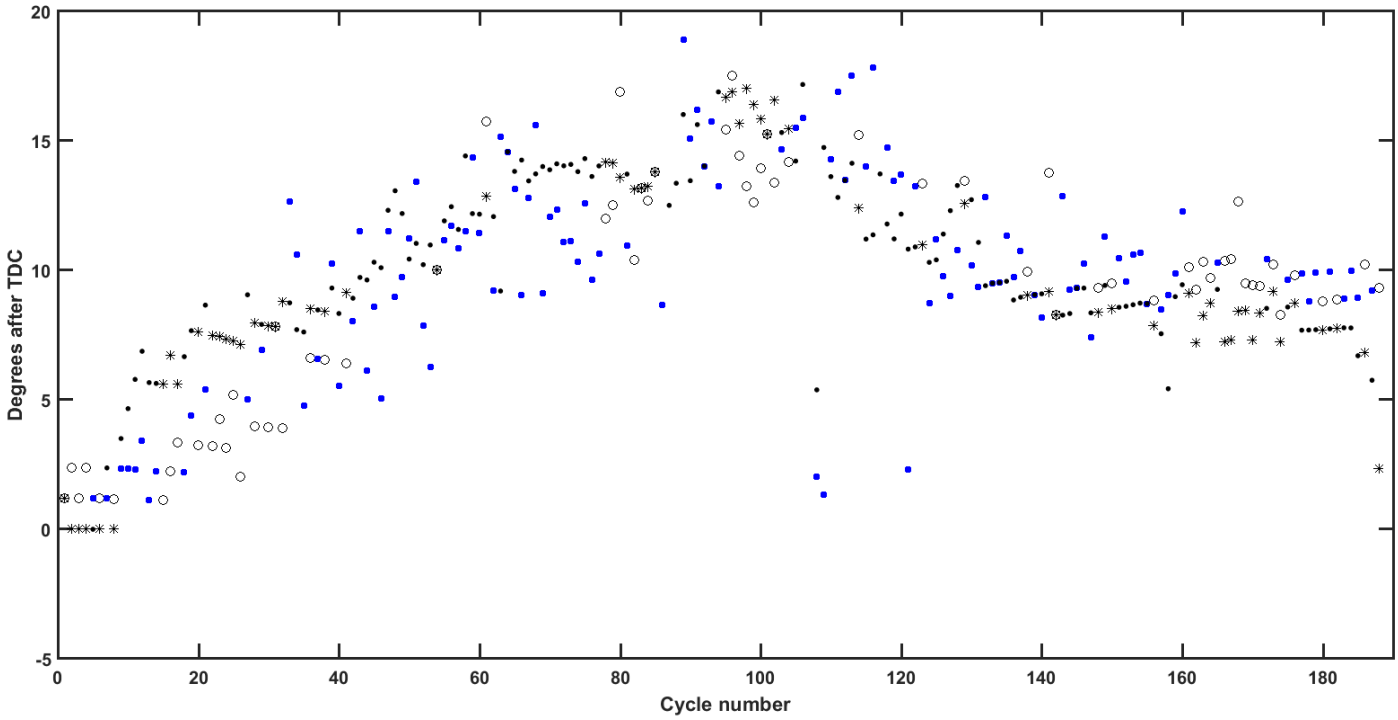

Figure 14. Locations of peak pressures for validation data including those ignored by the 'calibration peak pressure error' (equation (12)). Measured locations of peak pressure, 'o', predicted locations of peak pressures: '*', Measured locations of peaks ignored using the'calibration peak pressure error': '•', the discarded predicted of the locations of peak pressure for validation data '•'.

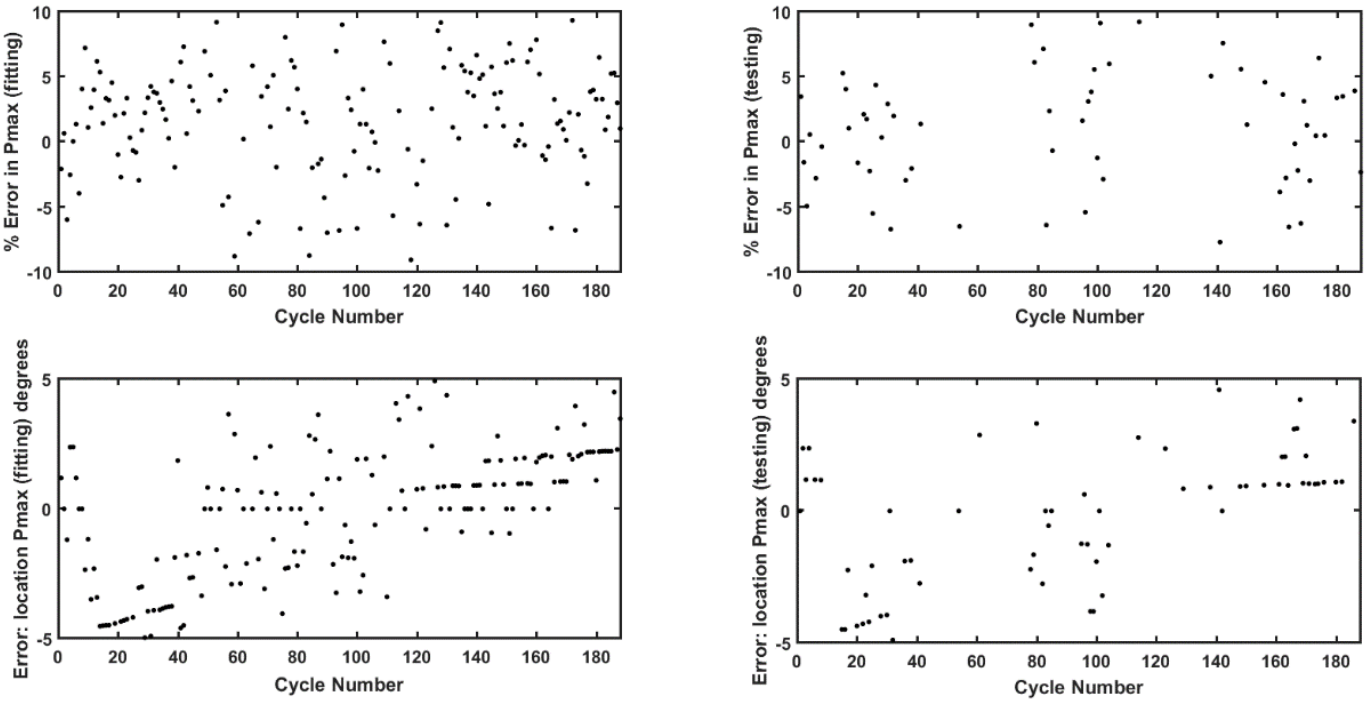

Figure 15. Prediction errors associated with peak pressure P_{max} and its location θ_{max} for the model fitting data (left), and all the previously unseen data (right) for which the 'calibration peak pressure error' (equation (12)) is satisfying the 3% acceptability criterion ΔP_{crit}=3.